ADVANCES IN ATMOSPHERIC SCIENCES, 2026

• **Original Paper** •

Can the Arctic Oscillation Be Used to Predict the Southern Indian Ocean Dipole Eight Months Ahead?

Yue SHI[1], Bin ZUO[2], Yazhou ZHANG[*1], Jianping LI[*1,3], Yang ZHAO[1], Yina DIAO[1], and Ting LIU[4,5]

[1]*State Key Laboratory of Physical Oceanography (POL)/Frontiers Science Center for Deep Ocean Multispheres and Earth System (FDOMES)/Key Laboratory of Physical Oceanography/Academy of the Future Ocean/College of Oceanic and Atmospheric Science, Ocean University of China, Qingdao, China*

[2]*PLA Dalian Naval Academy, Dalian, China*

[3]*Laboratory for Ocean Dynamics and Climate, Qingdao Marine Science and Technology Center, Qingdao, China*

[4]*State Key Laboratory of Satellite Ocean Environment Dynamics, Second Institute of Oceanography, Ministry of Natural Resources, Hangzhou, China*

[5]*Southern Marine Science and Engineering Guangdong Laboratory (Zhuhai), Zhuhai, China*

(Received 15 July 2025; revised 20 November 2025; accepted 2 December 2025)

ABSTRACT

Prediction of the southern Indian Ocean dipole (SIOD) used to rely on previous studies on the tropical variabilities, while the extratropical climate systems in the Northern Hemisphere may be unrepresented. This study finds a significant cross-seasonal influence of summer Arctic Oscillation (AO) on the SIOD in the subsequent boreal spring. During high summer AO years, high sea level pressure anomalies in the North Pacific favor the generation of anticyclonic anomalies locally. As a response, the easterly wind anomalies across the tropical Pacific are intensified, which amplifies the zonal dipole of sea surface temperature anomalies stretching the tropical Pacific, modulating the Walker circulation. Then, the surplus precipitation sustains from boreal summer to fall as a result of the anomalous convection coupled with the increased moisture over the western Pacific, which sets an advantageous stage for SIOD initiation through exciting cyclonic (anticyclonic) circulation over the eastern (western) pole of the SIOD in fall. The SIOD begins to grow in boreal winter in the context of the reinforcement of the heat fluxes and oceanic processes, and finally peaks in the following spring. On this basis, an empirical model using the preceding summer AO to predict the subsequent spring SIOD is established. The correlation coefficient between the predicted and observed SIOD is 0.5, which is slightly lower than that in the dynamical models from the North American Multi-model Ensemble Project (0.53), whereas the prediction skills of the former—in terms of the hit rate and false alarm rate—are much higher than the latter in predicting individual SIOD events.

Key words: southern Indian Ocean dipole, Arctic Oscillation, cross-seasonal influence, prediction

Citation: Shi, Y., B. Zuo, Y. Z. Zhang, J. P. Li, Y. Zhao, Y. N. Diao, and T. Liu, 2026: Can Arctic Oscillation predict the southern Indian Ocean dipole at 8-month ahead? *Adv. Atmos. Sci.*, https://doi.org/10.1007/s00376-025-5361-1.

Article Highlights:

- JJA AO provides a significant precursor signal for the SIOD up to eight months in advance.
- The model using JJA AO as the forecasting variable to predict SIOD events performs well.

1. Introduction

The southern Indian Ocean (SIO) plays a crucial role in the global climate system (Zhu et al., 2024), and it has high sensitivity to atmospheric switches due to the relative shallowness of its basin (Cai et al., 2007). The southern Indian Ocean dipole (SIOD), as the dominant interannual variability of the SIO, peaks from January to May. During its positive phase, the southwest part of the SIO experiences warm sea surface temperature (SST), while the northeastern part features cold SST, and vice versa in its negative phase (Behera and Yamagata, 2001). Numerous studies have also comprehensively concluded that SIOD events could have a substantial impact on climate variations across subtropical continents, such as southern Africa, Australia, India, and East Asia (Reason, 2001; Chen et al., 2023; Anila and Gnanaseelan, 2024; Guan et al., 2024). Consequently, improving the prediction of the SIOD can not only deepen our understanding of the internal physical mechanisms but can also have important implications for the mitigation of socioeconomic losses of the affected regions.

* Corresponding authors: Yazhou ZHANG, Jianping LI
Emails: zyz@ouc.edu.cn, ljp@ouc.edu.cn

Previous studies have reported that El Niño–Southern Oscillation (ENSO) demonstrates a remarkable correlation with the SIOD in terms of interannual variability when the former precedes the latter by about five months (Hermes and Reason, 2005). Crucially, the Walker circulation acts as an "atmospheric bridge" that intricately connects ENSO to the SST anomalies over the low-latitude SIO (0°–30°S), further facilitating the formation of the SIOD. However, for the central Pacific type of El Niño, the SIOD has since the 2000s become a key precursor with a 14-month lead (Jo et al., 2022). Moreover, the Indian Ocean dipole (IOD), featuring opposite variations of SST in the tropical Indian Ocean, exhibits a cyclic correlation with the SIOD. A positive SIOD can initiate the development of a positive IOD during the subsequent September–November (SON), while this positive IOD, in turn, serves as a crucial factor in triggering a negative SIOD event in the following January–March (JFM), thereby demonstrating a biennial oscillatory pattern (Gnanaseelan et al., 2012; Feng et al., 2014).

In addition, the dynamic linkage between the preceding extratropical signals in the Northern Hemisphere (NH) and the following tropical climate systems via air–sea interactions have been widely explored in many studies (Thompson and Wallace, 2000; Vimont et al., 2001; Alexander et al., 2010; Boschat et al., 2013; Ding et al., 2017). The primary variabilities of the sea level pressure (SLP) over the North Pacific, manifested as the first and second leading modes, are respectively known as the Aleutian low and the North Pacific Oscillation (Chiang and Vimont, 2004; Amaya, 2019; Jia et al., 2021). These two atmospheric modes, typically reaching their peaks in boreal winter or spring, can trigger subsequent winter ENSO within the framework of the seasonal footprinting mechanism (Vimont et al., 2003a, 2003b; Alexander et al., 2010; Yu and Kim, 2011; Chen et al., 2020, 2023; Ding et al., 2022). The Aleutian low can also be regarded as a significant Pacific center of action within the context of the Arctic Oscillation (AO; Thompson and Wallace, 2000; Honda et al., 2001; Li and Wang, 2003). The AO induces an anomalous anticyclone over the Aleutian region, accompanied by a distinct cyclonic anomaly. Simultaneously, warm SST and surplus precipitation occur over the subtropical North Pacific, triggering westerly wind anomalies over the tropical western central Pacific through the air–sea interaction, ultimately leading to the onset of the succedent winter El Niño (Nakamura et al., 2006, 2007; Zheng et al., 2021; Chen and Chen, 2022).

The aforementioned studies mostly focus on the impact of the AO on variabilities over the tropical Pacific and Indian Oceans. However, the possible ways by which the AO might impact the variability of the SIO remain unknown, and the potential links between the AO and SIOD are also in need of examination given the pronounced lead–lag relations of the AO and SIOD. Moreover, serving as a key precursor for SIOD forecasting, the AO is used to build an empirical prediction model for a lead time of approximately eight months.

The paper is structured as follows: Section 2 outlines the utilized data and methods. Section 3 shows the spatial and temporal relationships between the preceding summer AO and the subsequent spring SIOD, along with the underlying mechanism. The empirical prediction model that utilizes the AO as a key predictor for the SIOD is presented in section 4. Moreover, the performance of this model is evaluated by comparing its predictive skills with existing dynamical models derived from the North American Multi-model Ensemble (NMME). A summary and discussion are provided in section 5.

2. Datasets and methods

2.1. *Datasets*

The monthly data of SST in this study are from the Extended Reconstructed SST dataset, version 6 (ERSST.v6), based on the International Comprehensive Ocean–Atmosphere Dataset on a horizonal resolution of 2° × 2° (Huang et al., 2025a, 2025b). The SLP, horizonal winds at multiple pressure levels, vertical velocity, precipitation, longwave fluxes, and heat fluxes data are from the National Centers for Environmental Prediction–National Center for Atmospheric Research (NCEP–NCAR) reanalysis (Kalnay et al., 1996). The sea surface height (SSH) data are from the Simple Ocean Data Assimilation (SODA) reanalysis dataset, version 2.2.4, based on the assimilation of historical ocean observations into an ocean circulation model (Carton and Giese, 2008). The monthly mean AO index is from the Climate Prediction Center/National Oceanic and Atmospheric Administration (CPC/NOAA), which is defined as the leading principal component time series from an empirical orthogonal function analysis using SLP anomalies north of 20°N—the same as in Thompson and Wallace (2000).

The NMME is a collaborative seasonal climate prediction project developed by U.S. and Canadian institutes that integrates forecasts from multiple coupled atmosphere–ocean models (Kirtman et al., 2014), allowing us to evaluate the prediction skills of the AO-based model by comparing the predictability estimates between them within the same years. Eight models from the NMME project are utilized during 1986–2018. Each model comprises coupled ensemble members, and the forecasts are provided eight months ahead. Table 1 lists the key details of the models, including their abbreviated names, time periods, ensemble sizes, and lead times.

With reference to the conventional definition of the SIOD proposed by Behera and Yamagata (2001), and considering the regions that align well with the strongest and most coherent correlations between the AO and SST anomalies over the SIO, we choose (40°–53°S, 35°–44°E) and (12°–24°S, 75°–90°E) to represent the dipole regions of the SIOD. Therefore, the SIOD index is defined as the difference of the SST anomalies averaged within the western pole and the eastern pole. This adjustment is adopted to prioritize areas with robust AO–SIOD linkage, precisely capturing the

AO signals while preserving the essential characteristics of the SIOD. Then, using the threshold of one standard deviation, the SIOD events are categorized into three types: (1) positive cases when the amplitude exceeds one standard deviation; (2) negative cases when the amplitude falls short of one standard deviation; (3) neutral cases when the amplitude lies between. Here and throughout, we denote the year in which the AO peaks in June–August (JJA) as year(0) and the following year as year(+1).

2.2. *Methods*

The linear regression and correlation analysis methods are applied in this study, both of which are tested using two-tailed Student's *t*-tests. The empirical model is established through a holdout method (Devroye and Wagner, 1979), which depends on a single partitioning of the data. The time series is divided into two parts: the training period is from 1951 to 1985 and the hindcasting period spans from 1986 to 2018. The model is trained during the training period with the predictor variable, AO in JJA, regressed onto the dependent variable, the SIOD during the following February–April (FMA). This gives us the relation between the dependent variable, the SIOD, in the target season, and the predictor variable, the AO, at an eight-month lead during the hindcasting period.

The leave-one-out cross-validation method is applied to estimate the stability of the AO-model according to previous studies (Grantz et al., 2005), briefly introduced as follows: (1) Considering the original data with length L, one time point is retained as the validation data for testing the model, and the remaining subsample (length: L−1) is used to build the prediction model through regression analysis. (2) The ensemble hindcast is produced until each time point in the given time series has repeated step (1).

Table 2 shows the occurrence of observed and predicted SIOD events using the FMA SIOD for each individual model. Suggested by prior studies (Zhao et al., 2020; Zhang et al., 2024), the hit rates (in %) for correctly forecasting the occurrence of a positive/negative SIOD event (HRP and HRN, respectively) are defined as follows:

$$\mathrm{HRP} = \frac{a}{a+b+c} \times 100\,; \tag{1}$$

$$\mathrm{HRN} = \frac{i}{g+h+i} \times 100\,. \tag{2}$$

The false alarm rate (FAR; in %), which is a measure of incorrectly forecasting an SIOD event when in reality a neutral event occurred, is defined as follows:

$$\mathrm{FAR} = \frac{d+f}{d+e+f} \times 100\,. \tag{3}$$

The values of HRP, HRN, and FAR are given as percentages in the text.

3. Effect of the preceding summer AO on the following spring SIOD

3.1. *Spatiotemporal relationship between the AO and SIOD*

To identify the key season in which the AO exhibits a strongest relation with the FMA(+1) SIOD, a lead–lag correlation analysis between the FMA(+1) SIOD and the preceding three-month averaged AO index is conducted, as shown in Fig. 1a. The FMA(+1) SIOD has significant correlation coefficients with the preceding AO from May–July (MJJ) to July–September (JAS), with a peak in JJA when the latter leads the former by eight months (Fig. 1a). This suggests that a positive (negative) AO in the preceding JJA is typically followed by a positive (negative) SIOD in the following

Table 1. Details of the NMME climate models employed in this study.

Model	Period	Ensembles	Lead months
CanCM4i	Feb 1986–Apr 2018	10	8
CanSIPS-IC3	Feb 1986–Apr 2018	20	8
COLA-RSMAS-CCSM3	Feb 1986–Apr 2018	6	8
COLA-RSMAS-CCSM4	Feb 1986–Apr 2018	10	8
GEM-NEMO	Feb 1986–Apr 2018	10	8
GFDL-CM2p5-FLOR-A06	Feb 1986–Apr 2018	12	8
GFDL-CM2p5-FLOR-B01	Feb 1986–Apr 2018	12	8
NASA-GEOSS2S	Feb 1986–Apr 2018	4	8

Table 2. Forecasting positive, neutral, and negative SIOD events.

	Observed positive SIOD	Observed neutral event	Observed negative SIOD	Total
Forecasted positive SIOD	a	d	g	$a+d+g$
Forecasted neutral	b	e	h	$b+e+h$
Forecasted positive SIOD	c	f	i	$c+f+i$
Total	$a+b+c$	$d+e+f$	$g+h+i$	$a+b+c+d+e+f+g+h+i$

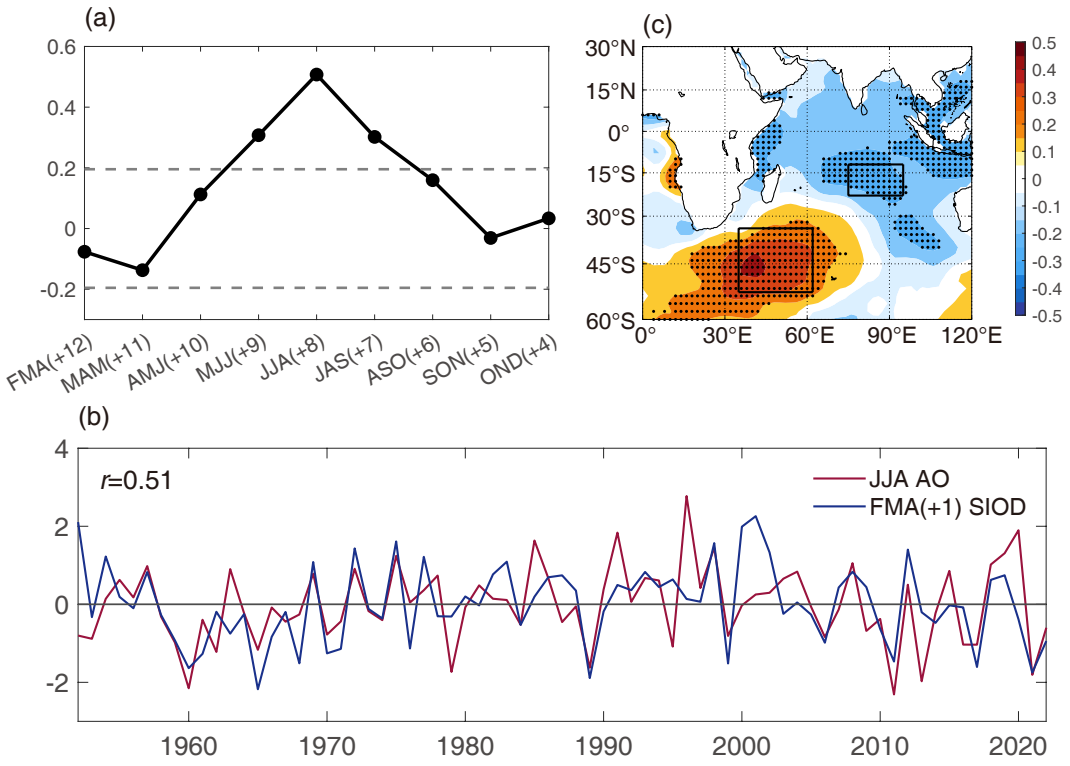

Fig. 1. (a) Lead–lag correlation coefficients between the FMA(+1) SIOD and the preceding overlapping three-month averaged AO. Numbers in parentheses denote the months by which the SIOD is led by the AO. (b) Time series of the standardized FMA(+1) SIOD (blue line) and JJA AO (red line) indices for the period 1951–2021, and the correlation coefficient (r = 0.51) between them is shown in the left top. (c) Correlation distributions between the JJA AO and the subsequent FMA SST anomalies in the SIO. The horizontal dashed lines in (a) represent the 90% confidence level. Dots in (c) show correlations significant above the 90% confidence level, and the boxes indicate the western and eastern poles of the SIOD.

FMA. The temporal correlation between the preceding JJA AO and the FMA(+1) SIOD is 0.51, exceeding the 99% confidence level (Fig. 1b). Moreover, Fig. 1c shows the spatial correlation of the preceding JJA AO and the FMA(+1) SST anomalies over the SIO. The SST anomalies associated with the preceding JJA AO feature a striking dipole pattern in the subsequent FMA (Fig. 1c), resembling the typical spatial structure of the SIOD.

Similar results can be obtained by employing other AO indices, i.e., the Northern Hemisphere Annular Mode (NAM) index, albeit with relatively smaller correlation coefficients [Fig. S1 in the electronic supplementary material (ESM)]. These results collectively demonstrate that the dominant atmospheric variability over the NH in JJA can exert reliable delayed influences on the following FMA SIOD, motivating us to explore the underlying physical mechanism that bridges them.

3.2. *Tropical Pacific air–sea interaction induced by the JJA AO*

How can the signal of the JJA AO be transmitted from the Arctic region to the SIO? The circulation variations over the tropical Pacific involved with oceanic processes may serve as the possible pathway modulating the close connections between the Arctic and the SIO (Chen et al., 2014). To verify this hypothesis, Fig. 2 displays the relationships of the JJA AO with the SST, 925-hPa wind, vertical velocity, and precipitation anomalies in JJA and SON.

The AO reflects a seesaw pattern in SLP anomalies between the Arctic and the midlatitudes (Thompson and Wallace, 1998; Shi and Nakamura, 2014; Choi et al., 2016). The large-scale AO-induced SLP anomalies represent an Aleutian low–like pattern (Fig. S2a in the ESM). To identify the associated circulation response, we analyze the relationships of this anomalous pattern with the SLP and 925-hPa wind anomalies. The results reveal that, during JAS, a remarkable high-pressure system dominates the central North Pacific, inducing an anomalous anticyclonic circulation and northeasterly winds branching from it propagating equatorward (Fig. S3a in the ESM). In August–October (ASO), despite the weakening and eastward displacement of the high-pressure, its southeastern component continuously enhances the equatorial easterlies (Fig. S3b in the ESM), until it collapses by SON (Fig. S3c in the ESM).

The tropical easterly anomalies contribute to the westward advection of the surface warm seawater over the western Pacific and the enhanced upwelling of the subsurface cold seawater over the tropical central-eastern Pacific (Fig. 2a), resulting in a prominent zonal SST gradient, which drives the anomalous Walker circulation (Fig. 2b). The enhanced con-

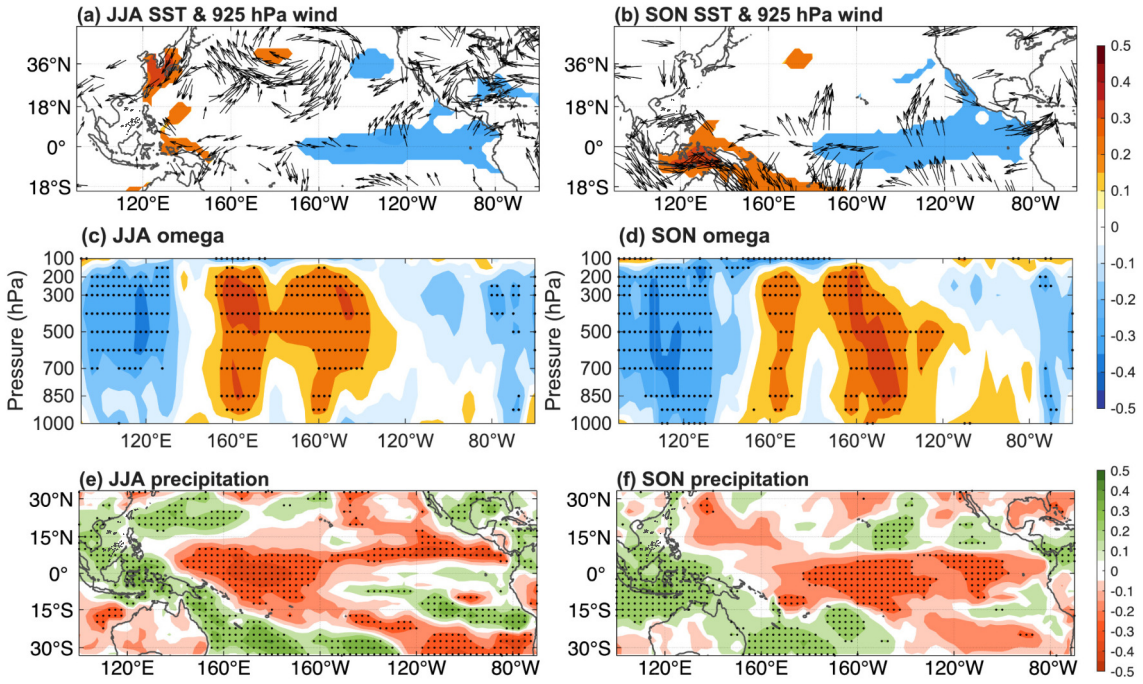

Fig. 2. (a) Regression of SST (shading; units: K) and 925-hPa wind (vectors; units: m s^{-1}) anomalies in JJA against the JJA AO. (b) As in (a) but for the SON SST and 925-hPa wind anomalies. (c–f) As in (a, b) but for the (c, d) vertical velocity (shading; units: Pa s^{-1}) averaged within 15°N–15°S and (e, f) precipitation (shading; units: mm d^{-1}) anomalies. Only regression coefficients significant above the 90% confidence level are shown in (a) and (b). Stippled areas in (c–f) pass the 90% confidence level.

vection coupled with the moisture influx over the warm pool generates surplus precipitation, while the suppressed convection, inhibiting the reduced moisture convergence produces a marked precipitation deficit over the eastern pool (Fig. 2c). Importantly, the anomalous precipitation pattern can in turn reinforce the zonal overturning circulation. Also, the atmosphere–ocean coupling exhibits strong persistence from JJA through SON (Figs. 2d–f).

3.3. *Maturation of the SIOD promoted by the JJA AO*

How does the tropical Pacific circulation variations associated with the JJA AO influence the subsequent FMA SIOD? The significant precipitation anomalies over the Maritime Continent may play a critical role in bridging the tropical Pacific and the Indian Ocean. The regression distributions of the SLP, 1000-hPa wind, SST, surface net downward longwave radiation flux, SSH, net latent heat flux, and net sensible heat flux anomalies against the preceding JJA AO spanning from SON to FMA are demonstrated.

As a response to the surplus precipitation over the Maritime Continent, Gill-type circulation develops in SON, with a pair of cyclones straddling the equator to the west of the Maritime Continent (Fig. 3a; Gill, 1980; Xing et al., 2014). The northern cyclone is partly weakened (Fig. 3a). However, the southern cyclone anchored over the eastern pole of the SIOD enhances low-level convergence and upward motion, which is balanced by upper-level divergent outflow and compensating subsidence to the western pole. This convective contrast establishes a prominent SLP dipole, fostering an anomalous anticyclone over the western pole (Fig. 3b).

In SON, the western SIOD pole begins to warm through strengthened downward longwave radiation (Fig. 4a), which intensifies both the latent heat and sensible heat fluxes (Figs. 5a, d), while the SST changes over the eastern pole are not so distinct (Fig. 3d). During DJF, the anticyclone over the western pole tends to weaken the climatological winds (Fig. S4b in the ESM), forming a wind–evaporation –SST mechanism (Xie and Philander, 1994; Amaya et al., 2017). The suppressed evaporation decreases the latent heat loss from the ocean (Fig. 5b), allowing for persistent warming of the western pole (Fig. 3e). Meanwhile, the shoaling thermocline favors cooling over the eastern pole (Fig. 4e), leading to a substantial SST dipole over the SIO (Fig. 3e). The warm SST anomalies over the western pole can sustain into FMA (Fig. 3f), while the oceanic configuration over the eastern pole amplifies due to the Bjerknes positive feedback (Fig. 4f; Bjerknes, 1969), which contributes to the peak of the SIOD in FMA (Fig. 3f). Overall, these processes serve as an atmosphere–ocean coupled bridge along which the preceding JJA AO can foster the maturation of the SIOD in the following FMA (Li et al., 2019).

4. Prediction of the SIOD in AO-based empirical and NMME models

Based on the physical linkage between the JJA AO and the following FMA SIOD, a new physics-based empirical

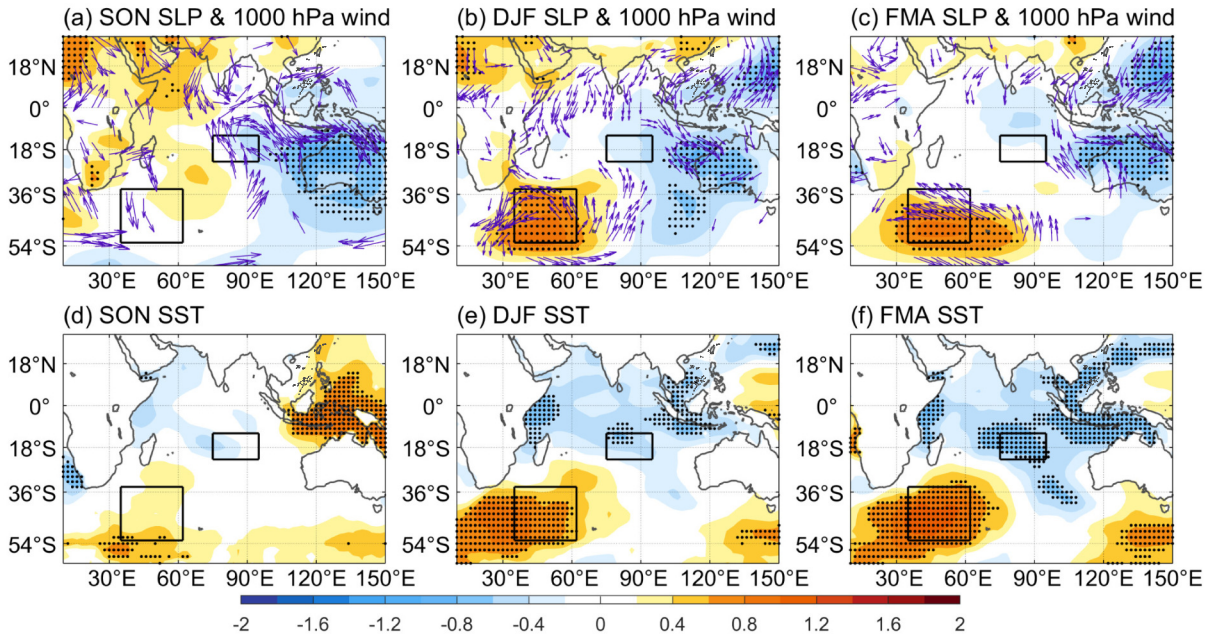

Fig. 3. (a) Regression of SLP (shading; units: hPa) and 1000-hPa wind (vectors; units: m s^{-1}) anomalies in SON against the preceding JJA AO. (b, c) As in (a) but for the (b) DJF and (c) FMA SLP and 1000-hPa wind anomalies. (d–f) As in (a–c) but for the SST (shading; units: K) anomalies. Stippled areas exceed the 90% confidence level, and only vectors significant above the 90% confidence level are shown in (a–c). The boxes indicate the western and eastern poles of the SIOD.

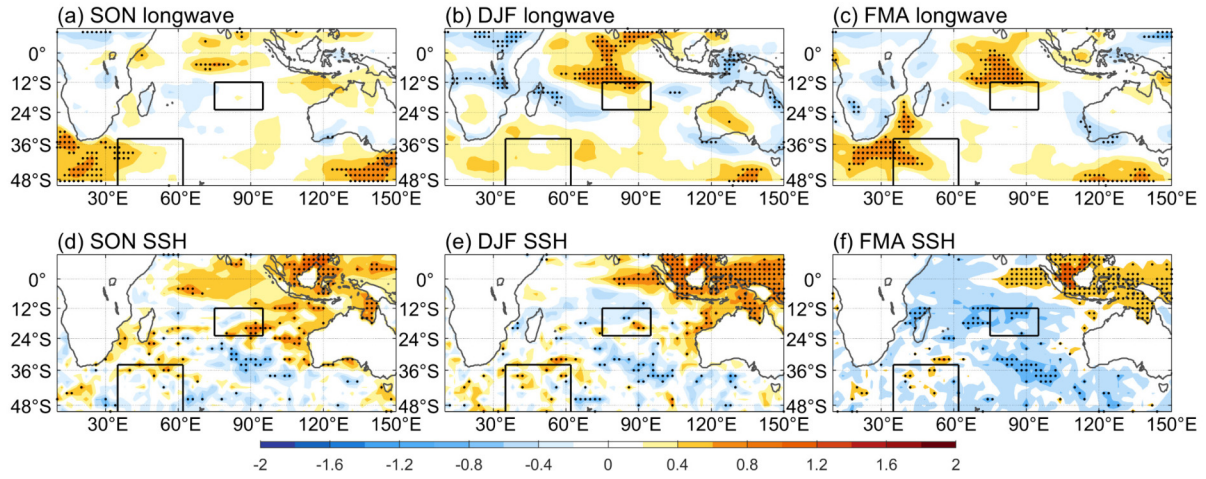

Fig. 4. (a) Regression of surface net downward longwave radiation flux (shading; units: W m^{-2}) anomalies in SON against the preceding JJA AO. (b, c) As in (a) but for the (b) DJF and (c) FMA longwave radiation flux anomalies. (d–f) As in (a–c) but for the SSH (shading; units: m) anomalies. Stippled areas exceed the 90% confidence level. The boxes indicate the western and eastern poles of the SIOD.

model is built through the holdout method (Devroye and Wagner, 1979), depending on the linear regression, which is named hereafter as the AO-model. The AO-model is trained during 1951–85 though the linear regression of the predictor variable, the AO, eight months earlier, onto the dependent variable, the SIOD, and thus the prediction model is expressed as follows:

$$\mathrm{SIOD}(t) = \omega \times \mathrm{AO}(t-8)\ , \qquad (4)$$

where t ($t-8$) is time (eight months earlier), and ω denotes the regression coefficient.

The AO-model is firstly tested with the leave-one-out cross-validation method (Fig. 6a), and the correlation coefficient between the observed and the cross-validated hindcast FMA(+1) SIOD indices is 0.5, passing the 99% confidence level, indicating the reliability of the AO-model. Then, employing the AO-model, the correlation between the observed and modeled SIOD index in FMA is 0.52 in the training period, exceeding the 99% confidence level (Fig. 6b). Although the correlation reduces slightly to 0.5 in the hindcast period, it is still significant above the 99% confi-

dence level (Fig. 6b). These results demonstrate the effective prediction skill of the AO-model.

Prior studies (e.g., Zhao et al., 2020; Zhang et al., 2024) have reported the superior prediction skills of the dynamical models from the NMME in evaluating climate variabilities (i.e., ENSO and the IOD). An assessment of the predictability of the SIOD in the AO-model through comparison with eight dynamical models is presented in Fig. 7a. A higher prediction skill for the temporal evolution of the SIOD in terms of both the correlation coefficient (0.5) and root-mean-square error (RMSE) (0.4) occurs in the AO-model than in all individual dynamical models from the NMME except for GFDL-CM2p5-FLOR-B01 (0.52 and 0.39). The prediction of the multi-model ensemble mean (MME, averaged across the eight NMME dynamical models) outperforms the AO-model, with a correlation coefficient of 0.53 and RMSE of 0.36 (Fig. 7a). This suggests that the SIOD predicted by the MME of the dynamical models is relatively superior to that predicted by the AO-model and individual dynamical models in the peak season.

To further evaluate the prediction skill for each culminated SIOD event, the positive and negative SIOD events are selected in the observations, AO-model, and dynamical model forecasts using one standard deviation in FMA, as displayed in Fig. 7b. The hit rate for the positive phase of the SIOD in the AO-model reaches 80%, which is much larger than that in all dynamical models and the MME forecast. By comparison, the AO-model performs much better in predicting positive SIOD events than negative SIOD events, whereas individual models exhibit better predictive skill for negative SIOD events, and half the dynamical models outperform the AO-model in predicting negative SIOD events (Fig. 7b). Regarding the false alarm rate, the AO-model performs better than both the individual dynamical models and

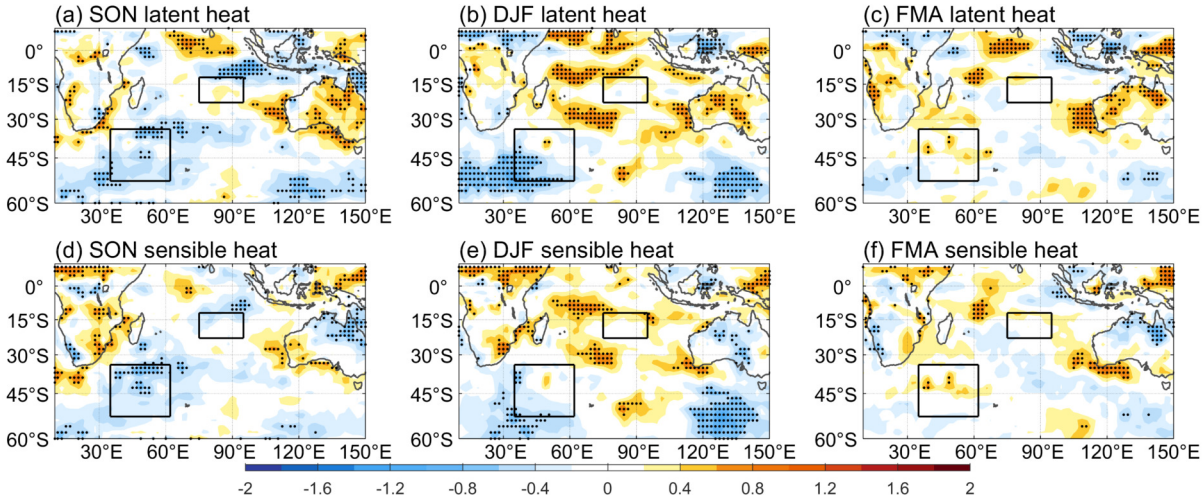

Fig. 5. (a) Regression of the net latent heat flux (shading; units: W m^{-2}) anomalies in SON against the preceding JJA AO. (b, c) As in (a) but for the (b) DJF and (c) FMA net latent heat flux anomalies. (d–f) As in (a–c) but for the net sensible heat flux (shading; units: W m^{-2}) anomalies. Positive values denote the upward direction. Stippled areas exceed the 90% confidence level. The boxes indicate the western and eastern poles of the SIOD.

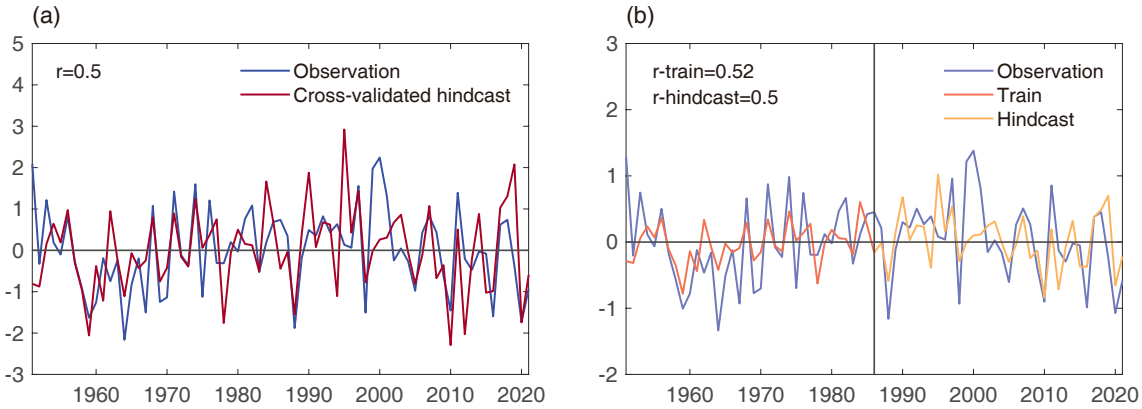

Fig. 6. (a) Standardized time series of the observed and leave-one-out cross-validation hindcast FMA(+1) SIOD index, with the correlation coefficient (r = 0.5) between them shown in the top left. (b) Time series of the observed (blue line), trained (orange line), and hindcasted (yellow line) FMA(+1) SIOD index. The correlations between the observed and modeled FMA(+1) SIOD indices during the training (r-train = 0.52) and hindcast (r-hindcast = 0.5) periods are shown in the top left.

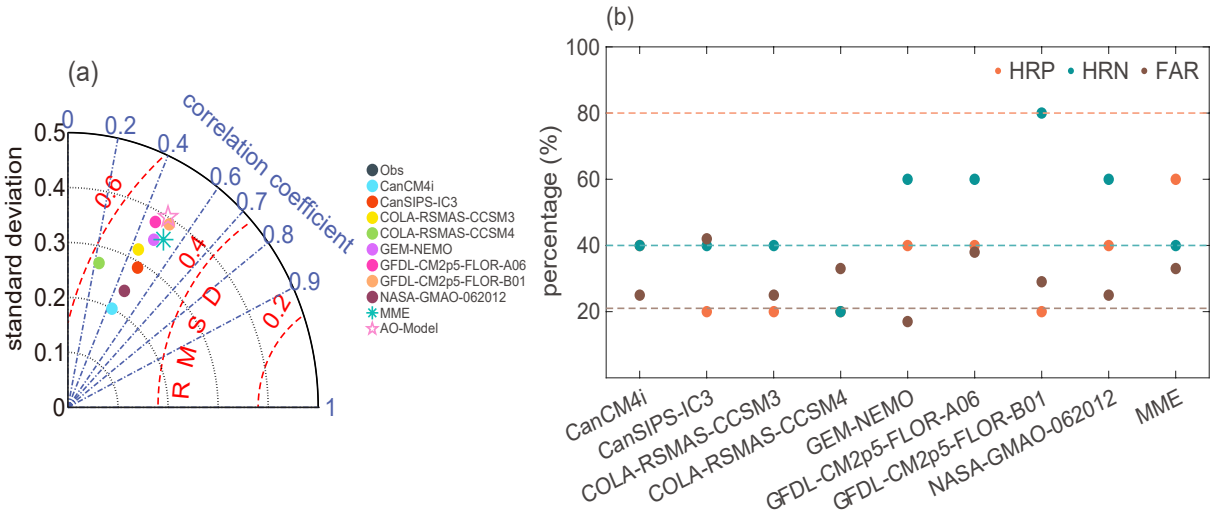

Fig. 7. (a) Taylor diagram of the predicted FMA(+1) SIOD based on eight dynamical models in the NMME (circles), the MME (green snowflake) averaged across the eight dynamical models, and the AO-model (pink pentagram) during the period 1986–2018. (b) Hit rates for the culminated positive (orange dots) and negative (green dots) SIOD events, along with the false alarm rates for both the culminated positive and negative SIOD events (brown dots), using individual dynamical models, MME hindcasts, and the AO-model (dashed lines).

the MME forecast, except for GEM-NEMO (Fig. 7b). These results demonstrate the prominent advantage of the physics-based AO-model in predicting the strong culminated SIOD events at an eight-month lead, in terms of both the hit rate and false alarm rate, relative to the dynamical models in the NMME.

5. Summary and discussion

The SIOD and its remote influences across the globe have gathered extensive attention due to its associations with the tropical Indian Ocean and the Asian monsoon (Anila and Gnanaseelan, 2024; Chen et al., 2024). Traditional diagnostic frameworks for SIOD prediction used to rely simply on the tropical variabilities, i.e., ENSO and the IOD, yet the extratropical climate systems may be unrepresented in previous studies, especially in the NH.

This study finds that the JJA AO may exert a cross-seasonal influence on the SIOD in the subsequent FMA, and the underlying mechanisms are investigated and illustrated in Fig. 8. A positive AO event in JJA typically generates a seesaw pattern in SLP anomalies between the Arctic and the Aleutian region, accompanied by an anomalous anticyclone over the North Pacific, which reinforces the equatorial easterly anomalies. The responsive zonal dipole of SST anomalies stretching the tropical Pacific promotes anomalous Walker circulation, thereby facilitating a dipole pattern of precipitation anomalies, which further advances the intensification of the Walker circulation. These circulation configurations can sustain from JJA to SON. The surplus precipitation over the Maritime Continent activates a Gill-type response, allowing an anomalous cyclone to form over the eastern pole of the SIOD in SON, along with an anomalous anticyclone over its western pole, preconditioning the SIOD's initiation. Then, the SIOD develops through DJF in the context of enhanced heat fluxes and oceanic processes, and finally peaks in the following FMA. Hence, we conclude that a positive AO in JJA is likely to trigger a positive SIOD event in the subsequent FMA through the atmosphere–ocean coupled bridge mechanism. Consistent results have been obtained with the Met Office HadISST and NOAA-CIRES-DOE Twentieth Century Reanalysis datasets (Rayner et al., 2003; Slivinski et al., 2019), confirming the robustness of the proposed physical process (Figs. S8–S12 in the ESM).

A simple empirical prediction model is then constructed with the AO serving as the predictor for the SIOD at a lead time of about eight months, and the predicted outputs generally simulate the variation of the SIOD. The leave-one-out cross-validation method is employed to test the robustness of the AO-model, and the relatively high correlation between the hindcasted and observed SIOD indicates that the AO is a promising parameter to be applied in SIOD forecasting. Additionally, advanced predictive skills compared to NMME models indicate far-reaching progress in predicting the SIOD.

A critical consideration for validating our AO–SIOD linkage is clarifying the role of ENSO. Firstly, to test whether the JJA AO is a downstream response of ENSO that affects the SIOD, we analyze the lead–lag correlation between ENSO and the JJA AO over a 24-month window. As shown in Fig. S5 in the ESM, ENSO exhibits no significant leading influence on the JJA AO, demonstrating that ENSO is not the initial driver. We then explore whether ENSO functions to transmit AO signals. Partial correlation analysis reveals that the relationship between the AO and the western pole remains robust after ENSO removal (Fig. S6 in the ESM), whereas the correlation between the AO and the eastern pole becomes statistically insignificant (Fig. S6 in the

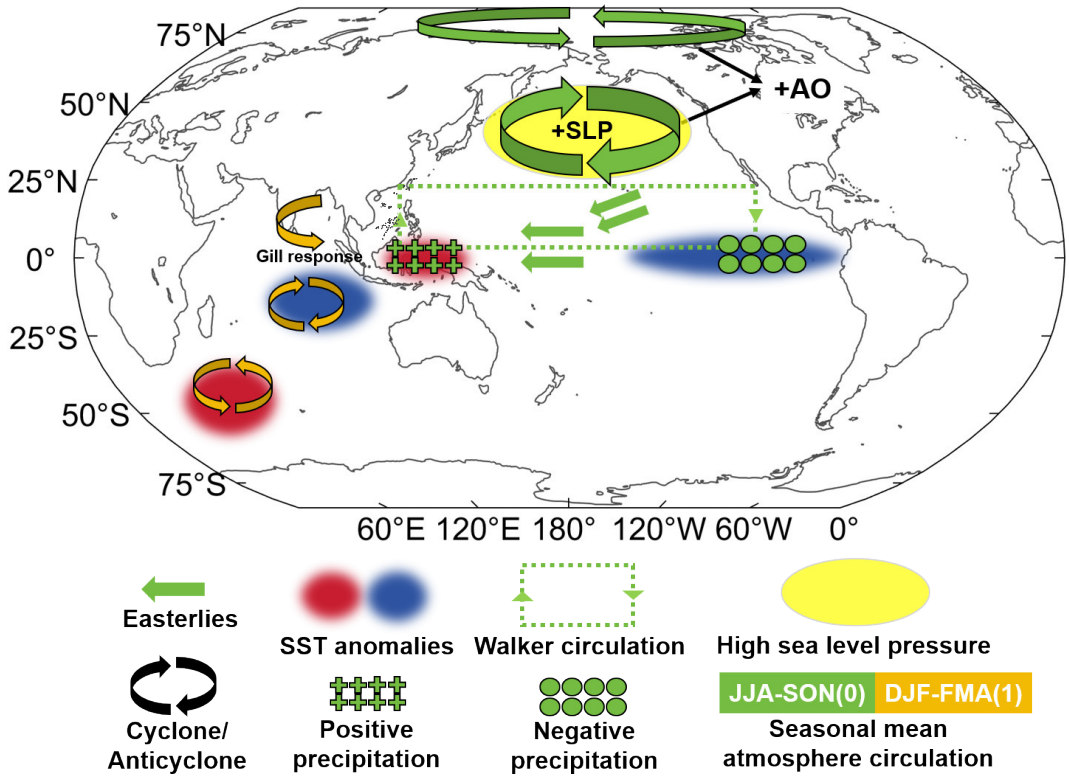

Fig. 8. Schematic illustrating the remote influence of a positive-phase AO during JJA on the SST anomalies of the SIO in the following FMA.

ESM), implying that ENSO could reinforce the AO's impact on the eastern pole, but is irrelevant to the western pole. Finally, to quantify ENSO's impact on SIOD prediction, we evaluate the performance of the AO-model after ENSO removal. The prediction skill declines after excluding ENSO signals but remains statistically significant (Fig. S7 in the ESM). These findings not only highlight the regulatory role of ENSO but also underscore the intrinsic contribution of the AO to the subsequent SIOD.

It is noteworthy that a pronounced AO-related signal also emerges over the eastern tropical Indian Ocean during the subsequent winter to spring, characterized by anomalously negative SST off Java. The affected regions closely correspond to the so-called "Java–Sumatra Niño/Niña" domain defined in earlier studies (Fig. S8 in the ESM; Lee et al., 2021, 2022), suggesting that the JJA AO may exert a prioritized influence on the development of the Java–Sumatra Niño/Niña. Correlation analysis indicates a possible linkage through anomalous offshore flows (Fig. S8 in the ESM). Nevertheless, the mechanisms involved warrant further detailed exploration.

Acknowledgements. Jianping LI was jointly supported by National Natural Science Foundation of China (NSFC) Project (42130607), Laoshan Laboratory (No. LSKJ202202600); Bin ZUO was supported by the National Natural Science Foundation of China (NSFC) Project (42305187); Yazhou ZHANG was sponsored by the Shandong Natural Science Foundation Project (ZR2024MD055).

Disclosure. ChatGPT 5.0 was used to improve the readability and language of the paper, but human authors were fully responsible for the content.

Data availability. ERSST.v6 was downloaded at https://www.downloads.psl.noaas.gov/Datasets/noaa.ersst.v6/; SODA 2.2.4 was derived from https://www.cen.uni-hamburg.de/en/icdc/data/ocean/easy-init-ocean/soda-224.html; the NCEP/NCAR reanalysis dataset is archived at https://psl.noaa.gov/data/gridded/data.ncep.reanalysis.html; the monthly mean AO index was obtained from http://www.cpc.ncep.noaa.gov; and NMME Forecasts of Monthly Climate Anomalies are available from www.cpc.ncep.noaa.gov/products/NMME/.

***Electronic supplementary material*:** Supplementary material is available in the online version of this article at https://doi.org/10.1007/s00376-025-5361-1.

REFERENCES

Alexander, M. A., D. J. Vimont, P. Chang, and J. D. Scott, 2010: The impact of extratropical atmospheric variability on ENSO: Testing the seasonal footprinting mechanism using coupled model experiments. *J. Climate*, **23**, 2885–2901, https://doi.org/10.1175/2010JCLI3205.1.

Amaya, D. J., 2019: The Pacific Meridional Mode and ENSO: A review. *Current Climate Change Reports*, **5**, 296–307, https://doi.org/10.1007/s40641-019-00142-x.

Amaya, D. J., M. J. DeFlorio, A. J. Miller, and S. P. Xie, 2017: WES feedback and the Atlantic Meridional Mode: Observa-

tions and CMIP5 comparisons. *Climate Dyn.*, **49**, 1665–1679, https://doi.org/10.1007/s00382-016-3411-1.

Anila, S., and C. Gnanaseelan, 2024: Evaluation of the Skill of CMIP6 models in simulating the interannual variability of Subtropical Indian Ocean SST in present climate. *Theor. Appl. Climatol.*, **155**, 8165–8183, https://doi.org/10.1007/s00704-024-05125-z.

Behera, S. K., and T. Yamagata, 2001: Subtropical SST dipole events in the southern Indian Ocean. *Geophys. Res. Lett.*, **28**, 327–330, https://doi.org/10.1029/2000GL011451.

Bjerknes, J., 1969: Atmospheric teleconnections from the equatorial Pacific. *Mon. Wea. Rev.*, **97**(3), 163--172, https://doi.org/10.1175/1520-0493(1969)097<0163:ATFTEP&linebreak/>gt;2.3.CO;2.

Boschat, G., P. Terray, and S. Masson, 2013: Extratropical forcing of ENSO. *Geophys. Res. Lett.*, **40**, 1605–1611, https://doi.org/10.1002/grl.50229.

Cai, W. J., T. Cowan, M. Dix, L. Rotstayn, J. Ribbe, G. Shi, and S. Wijffels, 2007: Anthropogenic aerosol forcing and the structure of temperature trends in the southern Indian Ocean. *Geophys. Res. Lett.*, **34**, L14611, https://doi.org/10.1029/2007GL030380.

Carton, J. A., and B. S. Giese, 2008: A reanalysis of ocean climate using Simple Ocean Data Assimilation (SODA). *Mon. Wea. Rev.*, **136**, 2999–3017, https://doi.org/10.1175/2007MWR1978.1.

Chen, J. S., Y. H. Guan, W. Zhou, X. H. Wu, Q. F. Lu, and X. Y. Li, 2024: Influence of the Southern Indian Ocean Dipole on the following spring climate in China: A synthetic observational and numerical study. *Atmospheric Research*, **299**, 107183, https://doi.org/10.1016/j.atmosres.2023.107183.

Chen, S. F., and W. Chen, 2022: Distinctive impact of spring AO on the succedent winter El Niño event: Sensitivity to AO's North Pacific component. *Climate Dyn.*, **58**, 235–255, https://doi.org/10.1007/s00382-021-05898-3.

Chen, S. F., B. Yu, and W. Chen, 2014: An analysis on the physical process of the influence of AO on ENSO. *Climate Dyn.*, **42**, 973–989, https://doi.org/10.1007/s00382-012-1654-z.

Chen, S. F., W. Chen, R. G. Wu, B. Yu, and H. F. Graf, 2020: Potential impact of preceding Aleutian low variation on El Niño–Southern Oscillation during the following winter. *J. Climate*, **33**, 3061–3077, https://doi.org/10.1175/JCLI-D-19-0717.1.

Chen, S. F., W. Chen, B. Yu, R. G. Wu, H. F. Graf, and L. Chen, 2023: Enhanced impact of the Aleutian Low on increasing the Central Pacific ENSO in recent decades. *npj Climate and Atmospheric Science*, **6**, 29, https://doi.org/10.1038/s41612-023-00350-1.

Chiang, J. C. H., and D. J. Vimont, 2004: Analogous Pacific and Atlantic Meridional Modes of tropical atmosphere–ocean variability. *J. Climate*, **17**, 4143–4158, https://doi.org/10.1175/JCLI4953.1.

Choi, Y. W., J. B. Ahn, and V. N. Kryjov, 2016: November seesaw in northern extratropical sea level pressure and its linkage to the preceding wintertime Arctic Oscillation. *International Journal of Climatology*, **36**(3), 1375--1386, https://doi.org/10.1002/joc.4431.

Devroye, L., and T. Wagner, 1979: Distribution-free performance bounds for potential function rules. *IEEE Transactions on Information Theory*, **25**, 601–604, https://doi.org/10.1109/TIT.1979.1056087.

Ding, R. B., I. S. Kang, R. Farneti, F. Kucharski, F. D. Sante, J. L. Xuan, F. Zhou, and T. Zhang, 2022: The internal and ENSO-forced modes of the Indian Ocean Sea surface temperature. *J. Climate*, **35**, 4191–4206, https://doi.org/10.1175/JCLI-D-21-0403.1.

Ding, R. Q., J. P. Li, Y. H. Tseng, C. Sun, and F. Xie, 2017: Joint impact of North and South Pacific extratropical atmospheric variability on the onset of ENSO events. *J. Geophys. Res.: Atmos.*, **122**, 279–298, https://doi.org/10.1002/2016JD025502.

Feng, J. Q., D. X. Hu, and L. J. Yu, 2014: How does the Indian Ocean subtropical dipole trigger the tropical Indian Ocean dipole via the Mascarene high. *Acta Oceanologica Sinica*, **33**, 64–76, https://doi.org/10.1007/s13131-014-0425-6.

Gill, A. E., 1980: Some simple solutions for heat-induced tropical circulation. *Quart. J. Roy. Meteor. Soc.*, **106**, 447–462, https://doi.org/10.1002/qj.49710644905.

Gnanaseelan, C., A. Deshpande, and M. J. McPhaden, 2012: Impact of Indian Ocean Dipole and El Niño/Southern Oscillation wind-forcing on the Wyrtki jets. *J. Geophys. Res.: Oceans*, **117**, C08005, https://doi.org/10.1029/2012JC007918.

Grantz, K., B. Rajagopalan, M. Clark, and E. Zagona, 2005: A technique for incorporating large-scale climate information in basin-scale ensemble streamflow forecasts. *Water Resour. Res.*, **41**, W10410, https://doi.org/10.1029/2004WR003467.

Guan, Y. H., J. S. Chen, Y. P. Wang, Y. Zhang, and X. Y. Li, 2024: Response of Indian Ocean intertropical convergence zone to southern Indian Ocean dipole. *Climate Dyn.*, **62**, 7445–7463, https://doi.org/10.1007/s00382-024-07288-x.

Hermes, J. C., and C. J. C. Reason, 2005: Ocean model diagnosis of interannual coevolving SST variability in the South Indian and South Atlantic Oceans. *J. Climate*, **18**, 2864–2882, https://doi.org/10.1175/JCLI3422.1.

Honda, M., H. Nakamura, J. Ukita, I. Kousaka, and K. Takeuchi, 2001: Interannual seesaw between the Aleutian and Icelandic lows. Part I: Seasonal dependence and life cycle. *J. Climate*, **14**, 1029–1042, https://doi.org/10.1175/1520-0442(2001)014<1029:ISBTAA>2.0.CO;2.

Huang, B. Y., and Coauthors, 2025a: Extended reconstructed sea surface temperature, version 6 (ERSSTv6). Part I: An artificial neural network approach. *J. Climate*, **38**, 1105–1121, https://doi.org/10.1175/JCLI-D-23-0707.1.

Huang, B. Y., and Coauthors, 2025b: Extended reconstructed sea surface temperature, version 6 (ERSSTv6). Part II: Upgrades on quality control and large-scale filter. *J. Climate*, **38**, 1123–1136, https://doi.org/10.1175/JCLI-D-24-0185.1.

Jia, F., W. J. Cai, B. L. Gan, L. X. Wu, and E. Di Lorenzo, 2021: Enhanced North Pacific impact on El Niño/Southern Oscillation under greenhouse warming. *Nature Climate Change*, **11**, 840–847, https://doi.org/10.1038/s41558-021-01139-x.

Jo, H. S., Y. G. Ham, J. S. Kug, T. Li, J. H. Kim, J. G. Kim, and H. Kim, 2022: Southern Indian Ocean Dipole as a trigger for Central Pacific El Niño since the 2000s. *Nature Communications*, **13**, 6965, https://doi.org/10.1038/s41467-022-34721-8.

Kalnay, E., and Coauthors, 1996: The NCEP/NCAR 40-year reanalysis project. *Bull. Amer. Meteor. Soc.*, **77**, 437–472, https://doi.org/10.1175/1520-0477(1996)077<0437:TNYRP>2.0.CO;2.

Kirtman, B. P., and Coauthors, 2014: The North American Multimodel Ensemble: Phase-1 seasonal-to-interannual prediction;

phase-2 toward developing intraseasonal prediction. *Bull. Amer. Meteor. Soc.*, **95**, 585–601, https://doi.org/10.1175/BAMS-D-12-00050.1.

Lee, S. K., and Coauthors, 2021: Java-Sumatra Niño/Niña and associate regional rainfall variability. *Research Square*, https://doi.org/10.21203/rs.3.rs-619357/v1.

Lee, S. K., and Coauthors, 2022: Java-Sumatra Niño/Niña and its impact on regional rainfall variability. *J. Climate*, **35**, 4291–4308, https://doi.org/10.1175/JCLI-D-21-0616.1.

Li, J. P., and J. X. L. Wang, 2003: A modified zonal index and its physical sense. *Geophys. Res. Lett.*, **30**, 1632, https://doi.org/10.1029/2003GL017441.

Li, J. P., F. Zheng, C. Sun, J. Feng, and J. Wang, 2019: Pathways of influence of the Northern Hemisphere Mid–high latitudes on East Asian climate: A review. *Adv. Atmos. Sci.*, **36**, 902–921, https://doi.org/10.1007/s00376-019-8236-5.

Nakamura, T., Y. Tachibana, and H. Shimoda, 2007: Importance of cold and dry surges in substantiating the NAM and ENSO relationship. *Geophys. Res. Lett.*, **34**, L22703, https://doi.org/10.1029/2007GL031220.

Nakamura, T., Y. Tachibana, M. Honda, and S. Yamane, 2006: Influence of the Northern Hemisphere annular mode on ENSO by modulating westerly wind bursts. *Geophys. Res. Lett.*, **33**, L07709, https://doi.org/10.1029/2005GL025432.

Rayner, N. A., D. E. Parker, E. B. Horton, C. K. Folland, L. V. Alexander, D. P. Rowell, E. C. Kent, and A. Kaplan, 2003: Global analyses of sea surface temperature, sea ice, and night marine air temperature since the late nineteenth century. *J. Geophys. Res.: Atmos.*, **108**, 4407, https://doi.org/10.1029/2002JD002670.

Reason, C. J. C., 2001: Subtropical Indian Ocean SST dipole events and southern African rainfall. *Geophys. Res. Lett.*, **28**, 2225–2227, https://doi.org/10.1029/2000GL012735.

Shi, N., and H. Nakamura, 2014: Multi-decadal modulations in the Aleutian-Icelandic Low seesaw and the axial symmetry of the Arctic Oscillation signature, as revealed in the 20th century reanalysis. *Tellus A: Dynamic Meteorology and Oceanography*, **66**, 22660, https://doi.org/10.3402/tellusa.v66.22660.

Slivinski, L. C., and Coauthors, 2019: NOAA-CIRES-DOE Twentieth Century Reanalysis Version 3. https://doi.org/10.5065/H93G-WS83.

Thompson, D. W. J., and J. M. Wallace, 1998: The Arctic Oscillation signature in the wintertime geopotential height and temperature fields. *Geophys. Res. Lett.*, **25**, 1297–1300, https://doi.org/10.1029/98GL00950.

Thompson, D. W. J., and J. M. Wallace, 2000: Annular modes in the extratropical circulation. Part I: Month-to-month variability. *J. Climate*, **13**, 1000–1016, https://doi.org/10.1175/1520-0442(2000)013<1000:AMITEC>2.0.CO;2.

Vimont, D. J., D. S. Battisti, and A. C. Hirst, 2001: Footprinting: A seasonal connection between the tropics and mid-latitudes. *Geophys. Res. Lett.*, **28**, 3923–3926, https://doi.org/10.1029/2001GL013435.

Vimont, D. J., D. S. Battisti, and A. C. Hirst, 2003a: The seasonal footprinting mechanism in the CSIRO general circulation models. *J. Climate*, **16**, 2653–2667, https://doi.org/10.1175/1520-0442(2003)016<2653:TSFMIT>2.0.CO;2.

Vimont, D. J., J. M. Wallace, and D. S. Battisti, 2003b: The seasonal footprinting mechanism in the Pacific: Implications for ENSO. *J. Climate*, **16**, 2668–2675, https://doi.org/10.1175/1520-0442(2003)016<2668:TSFMIT>2.0.CO;2.

Xie, S. P., and S. G. H. Philander, 1994: A coupled ocean-atmosphere model of relevance to the ITCZ in the eastern Pacific. *Tellus A: Dynamic Meteorology and Oceanography*, **46**(4), 340--350, https://doi.org/10.3402/tellusa.v46i4.15484.

Xing, N., J. P. Li, and Y. K. Li, 2014: A theoretical explanation of anomalous atmospheric circulation associated with ENSO Modoki during boreal winter. *Atmos. Ocean. Sci. Lett.*, **7**, 352–357, https://doi.org/10.3878/j.issn.1674-2834.14.0020.

Yu, J. Y., and S. T. Kim, 2011: Relationships between extratropical sea level pressure variations and the Central Pacific and Eastern Pacific types of ENSO. *J. Climate*, **24**, 708–720, https://doi.org/10.1175/2010JCLI3688.1.

Zhang, Y. Z., and Coauthors, 2024: Reconciling roles of the South China Sea summer monsoon and ENSO in prediction of the Indian Ocean dipole. *Environmental Research Letters*, **19**, 014041, https://doi.org/10.1088/1748-9326/ad122a.

Zhao, S., M. F. Stuecker, F. F. Jin, J. Feng, H. L. Ren, W. J. Zhang, and J. P. Li, 2020: Improved predictability of the Indian Ocean dipole using a stochastic dynamical model compared to the North American multimodel ensemble forecast. *Wea. Forecasting*, **35**, 379–399, https://doi.org/10.1175/WAF-D-19-0184.1.

Zheng, Y. Q., S. F. Chen, W. Chen, and B. Yu, 2021: Diverse influences of spring Arctic Oscillation on the following winter El Niño–Southern Oscillation in CMIP5 models. *Climate Dyn.*, **56**, 275–297, https://doi.org/10.1007/s00382-020-05483-0.

Zhu, L. G. N., and Z. W. Wu, 2024: Climatic influence of the Antarctic ozone hole on the East Asian winter precipitation. *npj Climate and Atmospheric Science*, **7**, 184, https://doi.org/10.1038/s41612-024-00732-z.